



- 1 -

1 **3D-printed microcell for protein NMR at high ionic strengths**  
2 **and small sample volumes**

3  
4

5 Tayeb Kakeshpour, Martin D. Gelenter, Jinfa Ying and Ad Bax

6

7 Laboratory of Chemical Physics, National Institute of Diabetes and Digestive and Kidney

8 Diseases, National Institutes of Health, Bethesda, MD 20892-0520, U.S.A.

9

10

11

12 *Not for publication:*

13 Contact: Ad Bax, email: bax@nih.gov

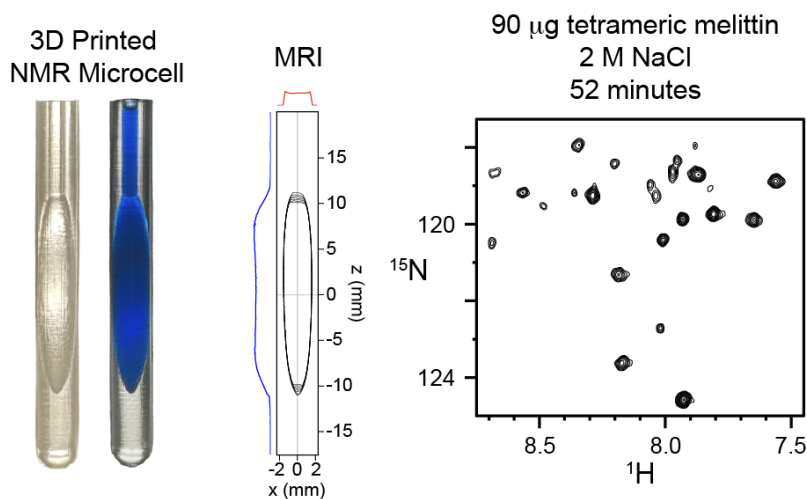
14 Building 5, room 126

15 NIH, Bethesda, MD 20892-0520

16 USA

17 Ph +1 301 496 2848

18





- 2 -

19 **Abstract.** Standard solution NMR measurements use 5-mm outer diameter (OD) sample  
20 tubes that require *ca* 0.5 mL of solvent to minimize “end effects” on magnetic field  
21 homogeneity in the active volume of the sample. Shigemi cells reduce the solvent  
22 requirement to *ca* 0.29 mL. At high ionic strength, or at ultrahigh magnetic fields, smaller  
23 OD samples are needed to study samples in conductive, radiofrequency absorbing solvents  
24 such as water. We demonstrate an effective and inexpensive alternative for reducing the  
25 active sample volume to 0.13 mL by 3D printing of ellipsoidal shaped cells that are inserted  
26 into 5-mm OD NMR tubes. Static magnetic susceptibility,  $\chi$ , of printer resin was measured  
27 using a simple slice-selection pulse sequence. We found that the  $\chi$  of water increases  
28 linearly with NaCl concentration, from -9.05 ppm to -8.65 ppm for 0 to 2 M NaCl. The  $\chi$   
29 of D<sub>2</sub>O was measured to be -9.01 ppm. The susceptibility difference between the resin ( $\chi$ =  
30 -9.40 ppm) and water can be minimized by paramagnetic doping of the resin. Such doping  
31 was found unnecessary for obtaining high quality protein NMR spectra when using  
32 ellipsoidal shaped cells that are insensitive to susceptibility mismatching. The microcells  
33 offer outstanding RF and good B<sub>0</sub> homogeneities. Integrated 600-MHz HSQC signal  
34 intensities for the microcell sample in PBS buffer were 6.5±4% lower than for 0.5 mL of  
35 the same protein solution in a regular 5-mm sample tube. The cell is demonstrated for N-  
36 acetylated  $\alpha$ -synuclein in PBS buffer, and for observing tetramerization of melittin at 2 M  
37 NaCl.

38

39

40

41



- 3 -

## 42 **1 Introduction**

43 Nearly all solution NMR measurements are carried out using standard 5-mm outer diameter  
44 (OD) sample tubes that require *ca* 0.5 mL of solvent to minimize “end effects” on magnetic  
45 field homogeneity in the active volume of the sample. Use of a Shigemitsu cell, which consist  
46 of glass with a magnetic susceptibility that is close to that of the selected solvent, can  
47 reduce the amount of sample required and thereby limit the cost of expensive protein  
48 preparations. However, the tubes are expensive and need to be matched to the magnetic  
49 susceptibility of the NMR solvent. The latter can be challenging considering that the  
50 susceptibility of water is somewhat temperature-dependent (Schenck, 1996) and increases  
51 substantially (becomes less negative) upon the addition of NaCl, whereas it increases by  
52 *ca* 0.04 ppm in D<sub>2</sub>O versus H<sub>2</sub>O (see below).

53 Magnetic susceptibility measurements of ionic solutions are often carried out using a  
54 magnetic field that oscillates at frequencies ranging from ~50 Hz to low MHz (Tsukada et  
55 al., 2006; Gutiérrez-Mejía and Ruiz-Suárez, 2012). However, for magnetic resonance  
56 purposes it is the magnetic susceptibility measured in a static magnetic field that is relevant  
57 to distortions in field homogeneity (Sangal et al., 2023) and to our efforts to develop a  
58 small volume sample cell for protein NMR.

59 We describe a simple method for measuring magnetic susceptibility of solid material in a  
60 high-resolution NMR spectrometer, and the development of a 3D printed microcell that  
61 can be inserted into a regular 5-mm NMR tube. The resin that we used for 3D printing at  
62 high resolution (25 μm) has a reported magnetic susceptibility of  $\chi = -9.34$  ppm (Sangal et  
63 al., 2023), which is well below that of water. However, by printing the cell with a spherical  
64 (Hizawa et al., 2017) or ellipsoidal geometry, magnetic field homogeneity within the cell  
65 becomes insensitive to the susceptibility mismatch between solvent and the printer resin  
66 (Schenck, 1996; VanderHart, 1996). The shape of our cell is perturbed by a narrow  
67 diameter, cylindrical access port that is needed to fill it with the NMR sample. Magnetic  
68 susceptibility mismatching effects, resulting from the deviation of a perfect ellipsoidal  
69 shape caused by this access port and by the finite resolution of the printer, can be minimized  
70 by paramagnetic doping of the printer resin with organic paramagnetic salt (Evans, 1959)  
71 but is found unnecessary for routine applications. The cells are reusable, but the cost of  
72 printing such cells is minimal and recycling them therefore may not be necessary.



- 4 -

73 The microcell is particularly useful for applications where the available sample quantity is  
74 limited, or when high ionic strength is required. High ionic strength lowers the quality  
75 factor (Q) of radiofrequency (RF) coils, and thereby negatively impacts NMR sensitivity,  
76 an effect that scales steeply with frequency (Ugurbil, 2018). RF penetration of water has  
77 been studied extensively for applications to magnetic resonance imaging, where it impedes  
78 the observation of tissue far from the body surface (Roschmann, 1987). RF absorption at  
79 high and ultrahigh magnetic fields also challenges solution  $^1\text{H}$  NMR spectroscopy, where  
80 the use of pulses that are compensated for both offset and RF inhomogeneity (Freeman et  
81 al., 1980; Xia et al., 2017) becomes essential, in particular for the vast majority of advanced  
82 experiments that include multiple  $180^\circ$  pulses (Manu et al., 2023). Use of the 3D printed  
83 microcell greatly reduces problems with probe detuning, lowering of Q, and RF absorption.  
84 Consequently, use of the microcell results in short  $^1\text{H}$  pulse widths with superior RF  
85 homogeneity, even at elevated ionic strength.

86 Analogous to a recent magnetic resonance imaging study of magnetic susceptibility of 3D  
87 printed materials (Sangal et al., 2023), we demonstrate simple methods for deriving  
88 magnetic susceptibility differences between ionic solutions and printer material in a high-  
89 field solution NMR magnet. We also demonstrate that while using only  $130\ \mu\text{L}$  of solvent,  
90 the sensitivity in common multi-dimensional NMR experiments, such as the gradient-  
91 enhanced HSQC (Kay et al., 1992), is comparable to what is obtained on a regular  $500\text{-}\mu\text{L}$   
92 sample. In another application, we show that high-quality spectra can be obtained for  $90$   
93  $\mu\text{g}$  of recombinantly expressed and chemically amidated melittin at  $2\ \text{M}$  NaCl  
94 concentration. Milligram-scale expression and purification of this uniformly  $^{15}\text{N}$ -enriched  
95 peptide in its post-translationally modified state, which tetramerizes in a salt-dependent  
96 manner, is expensive and very labor-intensive (Gelenter and Bax, 2023).

97

## 98 **2 Results and Discussion**

99

### 100 2.1 Measurement of magnetic susceptibility

101 For all materials pertinent to high-resolution solution NMR, the induced magnetization  $\mathbf{M}$   
102 depends linearly on the applied magnetic field  $\mathbf{H}_0$ :

$$103 \quad \mathbf{M} = \chi\mathbf{H}_0 \quad (1)$$



- 5 -

104 where  $\chi$  is the volume magnetic susceptibility, often expressed in units of parts per million  
105 (ppm), i.e.  $\chi$  is negative for diamagnetic media and positive for paramagnetic substances.  
106 The magnetic flux density,  $\mathbf{B}_0$ , is directly proportional to  $\mathbf{H}_0$ :

$$107 \quad \mathbf{B}_0 = \mu \mathbf{H}_0 \quad (2)$$

108 where the magnetic permeability  $\mu$  corresponds to  $\mu = (1+\chi)\mu_0$ , and  $\mu_0 = 4\pi \cdot 10^{-7}$  H/m is  
109 the permeability of vacuum. In an NMR sample, the magnetic flux density corresponds to  
110 the sum of the applied magnetic field  $\mathbf{H}_0$  and the integral of the magnetic field contributions  
111 from the induced magnetization over all sample volume elements at locations  $\mathbf{r}$  relative to  
112 the point of interest. For a cylindrical sample of infinite length, with its axis parallel to a  
113 homogeneous applied magnetic field, the integral over all space within the cylinder is  
114 uniform across all locations, resulting in

$$115 \quad \mathbf{B}_0 = \mu_0(1+\chi) \mathbf{H}_0 \quad (3)$$

116 Magnetic flux is conserved at any interface orthogonal to  $\mathbf{H}_0$  between two media with  
117 magnetic susceptibilities  $\chi_1$  and  $\chi_2$ . For the example of a Shigemi sample cell, where the  
118 bottom segment of the cylindrical tube consists of glass with susceptibility  $\chi_g$ , and  $\chi_s$  is the  
119 solvent susceptibility above it (Figure 1A), the flux density at the interface is given by

$$120 \quad \mathbf{B}_0 = \mu_0[1 + (\chi_g + \chi_s)/2] \mathbf{H}_0 \quad (4)$$

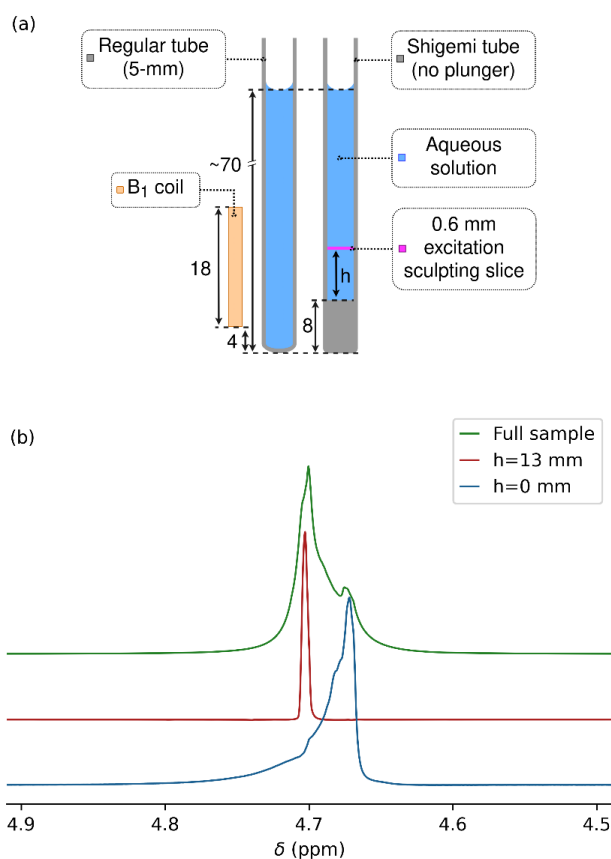
121 Away from the interface, the integrated contributions to  $\mathbf{B}_0$  from volume elements below  
122 and above the interface depend on the height above the interface as well as the transverse  
123 location, with values converging to  $\mathbf{B}_0 = \mu_0(1 + \chi_s)\mathbf{H}_0$  at distances above the interface that  
124 are large relative to the tube inner diameter,  $D$ . Therefore, when selectively observing  
125 solvent signal with a chemical shift of  $\delta_0$  from a very thin slice perpendicular to the sample  
126 axis at height  $h$  above the interface (Figure 1A), a narrow signal at a frequency  $\delta(h) = [1 +$   
127  $(\chi_g + \chi_s)/2]\delta_0$  is observed for  $h \ll D$ , with  $\delta(h)$  approaching  $(1 + \chi_s)\delta_0$  for  $h \gg D$ , and a  
128 complex line shape for slices taken at intermediate values.

129 Hence, for a solution above the solid glass of a Shigemi cell with a total solvent height that  
130 is large relative to both  $D$  and the height of the receiver coil, the line shape corresponds to  
131  $\delta(h)$  contributions ranging from  $[1 + (\chi_g + \chi_s)/2]\delta_0$  to  $(1 + \chi_s)\delta_0$ . In other words, the total



- 6 -

132 width of the line shape at its base corresponds to half the difference between  $\chi_g$  and  $\chi_s$  in  
133 units of ppm.



134

135 **Figure 1.** Measurement of magnetic susceptibility in a Shigemi sample tube. (A) Prior to  
136 measurements on this sample, the magnetic field homogeneity was optimized for a regular 5-mm  
137 NMR sample tube, filled to the same height of 70 mm above the bottom of the tube, and inserted  
138 to the same depth into the probehead. Dimensions in mm. A thin slice (pink) through the sample  
139 at height  $h$  above its bottom was selected by excitation sculpting. (B) HDO resonances for the  
140 Shigemi sample tube containing 0.3% H<sub>2</sub>O/99.7% D<sub>2</sub>O (no plunger). The glass/liquid interface of  
141 the Shigemi cell was positioned 5 mm below the center of the receiver coil, using the shim settings  
142 of a regular 5-mm sample tube filled to the same total height with the same solution, inserted  
143 to the same depth into the NMR probe (see left half of panel A). Overlaid are spectra recorded for  
144 the entire sample (green) and for 0.6-mm thickness horizontal slices through the Shigemi cell,  
145 centered at  $h = 0$  mm (blue), and at  $h = 13$  mm (red) by using excitation sculpting while applying  $z$   
146 gradients.

147



- 7 -

148 2.2 Measurement of magnetic susceptibility in a high-resolution NMR magnet

149 Careful measurements of solvent susceptibility in a high-resolution magnet that used the  
150 gas phase of TMS as an internal reference have been reported by Hoffman (Hoffman,  
151 2020;Hoffman, 2022). Here, we describe a different approach that also permits  
152 susceptibility measurements of solid objects. First, we demonstrate the method for  
153 measurement of the susceptibility of the glass bottom section of a Shigemi cell.

154 Bruker's topshim program was used to minimize magnetic field inhomogeneity of a regular  
155 5-mm sample that contained a 1-mL solution of a variable NaCl concentration in 97%  
156 D<sub>2</sub>O/3% H<sub>2</sub>O, that was inserted into the probe to have its bottom ~13 mm below the center  
157 of the receiver coil. Then, without changing the shim settings, the HDO line shape on the  
158 same solvent composition was observed for a Shigemi sample tube, inserted to the same  
159 depth into the probehead. Because the Shigemi tube had an 8-mm bottom segment of solid  
160 glass, the flat solvent-glass interface then is located 5 mm below the center of the receiver  
161 coil (Figure 1A). If  $\chi_g$  were identical to  $\chi_s$ , the same perfect line shape would be expected,  
162 but with approximately 15% lower intensity because the bottom ~15% of the receiver coil  
163 now was filled with solid glass from the Shigemi tube.

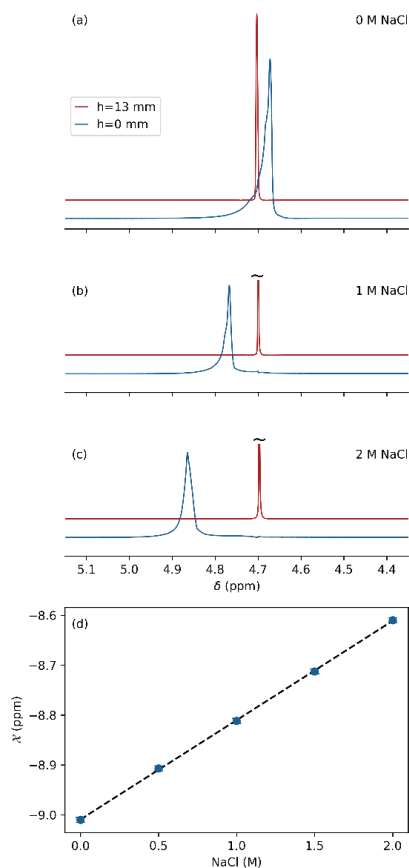
164 For the 97% D<sub>2</sub>O/3% H<sub>2</sub>O Shigemi tube sample, a pronounced upfield shoulder was  
165 observed (Figure 1B, green), indicative of susceptibility mismatching. Excitation sculpting  
166 (Stott et al., 1995) (Appendix A1) while applying a pulsed  $z$ -gradient was then used to  
167 select a slice of 0.6-mm thickness, centered at the glass-solvent interface, i.e. selecting a  
168 ~0.3-mm solvent layer just above the interface. A resonance for this layer was observed  
169 that was 0.032 ppm upfield from the most intense segment of the solvent obtained with a  
170 30° pulse, without slice selection (Figure 1B). When selecting a slice at a height of 13 mm  
171 above the interface, the signal (Figure 1B, red) coincided with the maximum of the  
172 resonance obtained without slice selection. Therefore, the difference in frequency between  
173 the red and blue resonances provides a good measure for the difference between  $(\chi_g + \chi_s)/2$   
174 and  $\chi_s$ .

175 Repeating the same measurement but using 97% H<sub>2</sub>O/3% D<sub>2</sub>O and strongly mistuning the  
176 probehead to reduce radiation damping, showed a shoulder that was 0.0183 ppm closer to



- 8 -

177 the frequency observed 8 mm above the center of the coil (i.e.  $h = 13$  mm; Appendix A2).  
178 Accounting for the solutions not being fully deuterated or protonated, their difference in  
179 static magnetic susceptibility then equals  $\chi_{\text{H}_2\text{O}} - \chi_{\text{D}_2\text{O}} = 2 \times 0.0183 \times (100/94) = 0.04$  ppm. The  
180 widely used literature value for  $\chi_{\text{H}_2\text{O}}$  is -9.05 ppm (Sangal et al., 2023), yielding  $\chi_{\text{D}_2\text{O}} = -$   
181 9.01 ppm, in fair agreement with Hoffman's measurements (Hoffman, 2022). Using  $\chi_{\text{D}_2\text{O}}$   
182 = -9.01 ppm as a reference, the susceptibility of the Shigemi glass used in our  
183 measurements is  $\chi_{\text{g}} = -9.08$  ppm.



184

185 **Figure 2.** Effect of salt on magnetic susceptibility of 97%  $\text{D}_2\text{O}$ . Resonances shown correspond to a  
186  $\approx 0.6$ -mm thick slice through a Shigemi tube, centered at  $h = 0$  (blue) and  $h = 13$  mm (red)  
187 above the glass bottom of the Shigemi sample cell, using the same protocol as for Figure 1B at (A) 0 mM  
188 NaCl; (B) 1.0 M NaCl; (C) 2.0 M NaCl. (D) Magnetic susceptibility of  $\text{D}_2\text{O}$  as a function of NaCl  
189 concentration, using  $\chi_{\text{D}_2\text{O}} = -9.01$  ppm as a reference. The intensities of the slices at  $h = 0$  are  
190 upscaled  $\approx 16$ -fold to account for the 50% smaller aqueous volume and the strong magnetic field  
191 inhomogeneity in these lower slices.





- 9 -

### 192 2.3 Salt dependence of water magnetic susceptibility

193 The effect of dissolved NaCl on magnetic susceptibility of water is important to protein  
194 NMR. We therefore repeated the above measurements of the 97% D<sub>2</sub>O/3% H<sub>2</sub>O Shigemi  
195 tube sample after addition of 0.5, 1, 1.5, and 2 M analytical grade NaCl (Sigma-Aldrich)  
196 to the solvent (Figure 2A-C), showing a linear increase in solvent susceptibility with salt  
197 concentration over this range:  $\chi_{\text{D}_2\text{O}+\text{NaCl}} = -9.01 + [\text{NaCl}] \times 0.2$  ppm, where [NaCl] denotes  
198 the concentration molarity (Figure 2D).

### 199 2.4 Susceptibility and paramagnetic doping of 3D printer resin

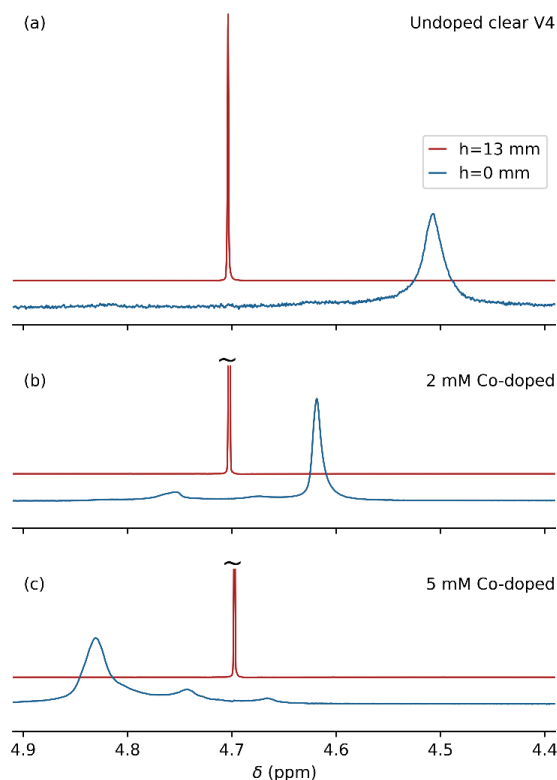
200 Clear V4 resin was used because it enabled the highest precision (25- $\mu\text{m}$  resolution) of  
201 printing on a FormLabs Form3+ 3D printer available in our laboratory, and its optical  
202 transparency facilitated sample handling for 3D printed microcells. The susceptibility of  
203 the printed Clear V4 resin was measured in the same manner as described above for the  
204 Shigemi tube. A cylindrical plug of 2 cm length was printed and pushed to the bottom of  
205 a standard 5-mm NMR sample tube that was prefilled with 0.7 mL 1% H<sub>2</sub>O/99% D<sub>2</sub>O,  
206 such that the top of the plug was again 5 mm below the center of the receiver coil once  
207 inserted into the magnet. Shimming of the magnetic field was carried out on a sample  
208 without the plug, filled to the same level by using  $\sim 1$  mL of the same solvent, inserted into  
209 the probehead at the same depth, i.e. with the bottom of the sample tube at 25 mm below  
210 the center of the RF coil.

211 The frequency difference observed at the D<sub>2</sub>O/resin interface versus the top of the coil was  
212  $-0.195$  ppm (Figure 3A), corresponding  $\chi_{\text{ClearV4}} = -9.40$  ppm, which is close to the value  
213 of  $-9.33$  ppm measured for this resin by magnetic resonance imaging (Sangal et al., 2023).  
214 Considering that a mismatch in magnetic susceptibility between the sample cell and the  
215 solution impacts the achievable B<sub>0</sub> homogeneity, and that  $\chi_{\text{ClearV4}} < \chi_{\text{H}_2\text{O}}, \chi_{\text{D}_2\text{O}}$ , increasing  
216 the value of  $\chi_{\text{ClearV4}}$  by paramagnetic doping of the resin in principle allows elimination of  
217 this difference. Finding a paramagnetic doping substance that is miscible with the printer  
218 resin and does not impact the performance of the 3D printer proved challenging. For  
219 example, the use of concentrated CuCl<sub>2</sub> in methanol strongly impacted the polymerization



- 10 -

220 kinetics The same problem was encountered for a range of strong paramagnetic chelated  
221 substances, such as gadodiamide (Omniscan), which is commonly used in protein  
222 paramagnetic relaxation enhancement measurements and as a contrast agent in magnetic  
223 resonance imaging. However, the hydrophobic cobalt(II) complex, cobalt(II) bis(2-  
224 ethylhexanoate), available from Sigma-Aldrich as a 65 wt. % solution in mineral spirits  
225 (product number: 444545), proved miscible with the Clear V4 printer resin without major  
226 adverse impact on print quality.



227

228 **Figure 3.** Effect of cobalt(II)2-ethylhexanoate doping on the magnetic susceptibility of printed  
229 Formlabs Clear V4 resin. A solid plug of printed resin that is 2 cm in length and has a 4.0-mm outer  
230 diameter (OD) was inserted into a regular 5mm OD NMR sample tube (Wilmad-507; ID 4.2 mm),  
231 prefilled with 0.7 mL 99%D<sub>2</sub>O/1%H<sub>2</sub>O. Overlaid spectra are shown from 0.6-mm thickness slices  
232 centered at the top of a Clear V4 plug (blue), and 13 mm above the plug (red). (A) No doping; (B)  
233 2 mM cobalt(II) doping; (C) 5 mM cobalt(II) doping.



- 11 -

234 Comparison of the difference in HDO resonance frequencies obtained for slices at 13 mm  
235 above the interface between solvent and printed plug and at the interface for three different  
236 levels of the cobalt(II) doping, 0 mM (Figure 3A); 2 mM (Figure 3B) and 5 mM (Figure  
237 3C), shows a doping-dependent decrease from +117 Hz to -80 Hz for the NaCl-free 99%  
238 D<sub>2</sub>O sample. This result indicates that it is possible to match the susceptibility of the solvent  
239 to that of the printed resin. However, that would require a large number of printed cells to  
240 cover the ionic strength range from 0 to 2 M salt, while also accounting for the difference  
241 between D<sub>2</sub>O and H<sub>2</sub>O samples.

242 In practice, printing sample cells with different levels of cobalt(II) doping is labor-intensive  
243 because it requires thorough cleaning of the printing vat used by the Formlabs 3D laser  
244 printer. Printing with doped resin requires mixing of the viscous resin at the molecular level  
245 with the doping agent and keeping it homogenous during printing. The latter also required  
246 some modification of the printer to prevent refreshing of the printer resin with undoped  
247 resin from a sealed cassette during printing. We therefore resorted to printing the sample  
248 cells with an ellipsoidal shape, that to a good approximation were insensitive to the  
249 susceptibility mismatch between solvent and printed resin (Schenck, 1996; VanderHart,  
250 1996).

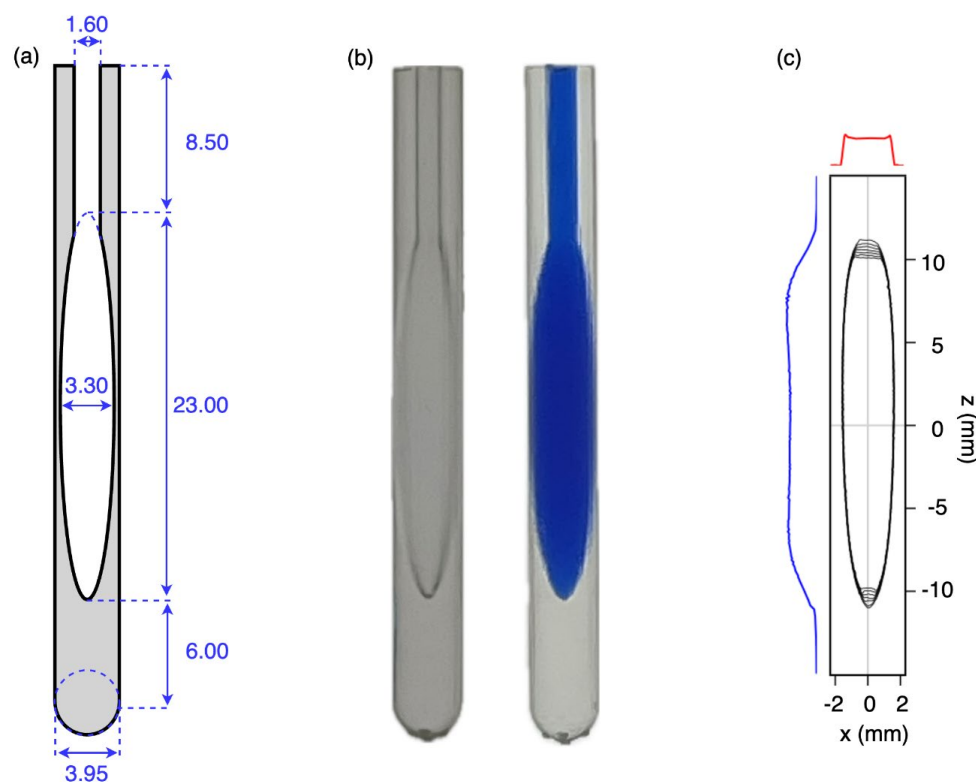
#### 251 2.4 Performance of a Clear V4 ellipsoidal microcell

252 For applications to proteins, we settled on an ellipsoidal microcell design with a volume of  
253 130  $\mu$ L (Figure 4A). A printed access channel of 1.6 mm diameter (measured 1.3 mm) and  
254 8.5-mm length and a volume of  $\sim$ 11  $\mu$ L was used for cleaning of the sample after the initial  
255 print and prior to further hardening of the resin in a Formlabs light chamber (see Methods).  
256 A subsequent overnight rinse with Milli-Q H<sub>2</sub>O at 60 °C was used to remove small water-  
257 soluble contaminants that otherwise remain on the inside surface of the cell. For  
258 applications to samples in D<sub>2</sub>O, leaving the sample filled with D<sub>2</sub>O can be used to reduce  
259 the intensity of a weak, very broad ( $\sim$ 1 kHz) signal at  $\sim$ 3.8 ppm, that appears to result from  
260 H<sub>2</sub>O diffusing into the resin. Because the digital printer increases the size of printed parts  
261 by a small amount due to partial polymerization adjacent to the laser-selected spots, the  
262 printed walls of the chamber are actually slightly thicker than designed, and the total



- 12 -

263 volume of the cell including its access channel was measured gravimetrically to be 130  $\mu\text{L}$   
264 (Figure 4B).



265  
266

267 **Figure 4.** Images of the printed microcell. (A) Technical drawing; note that the actual dimensions  
268 of printed material are slightly larger due to polymerization of a thin ( $\sim 0.15$  mm) sticky surface  
269 layer that remains on the printed cell prior to subsequent UV curing. (B) Photographs of the  
270 printed cells (left) prior to and (right) after filling with a blue dye solution; (C) Contour plot of a  
271 sagittal  $xz$  cross-section through a 3D image of a 97%  $\text{D}_2\text{O}$ , 3%  $\text{H}_2\text{O}$  sample containing 1.8 mM  
272  $\text{CuCl}_2$  to shorten the  $^1\text{H} T_1$  value to  $\sim 0.7$  s. The image was recorded in absorption mode on an 800-  
273 MHz NMR spectrometer equipped with a 3-axis pulsed field gradient probehead. The total  
274 measurement time was 9 minutes.

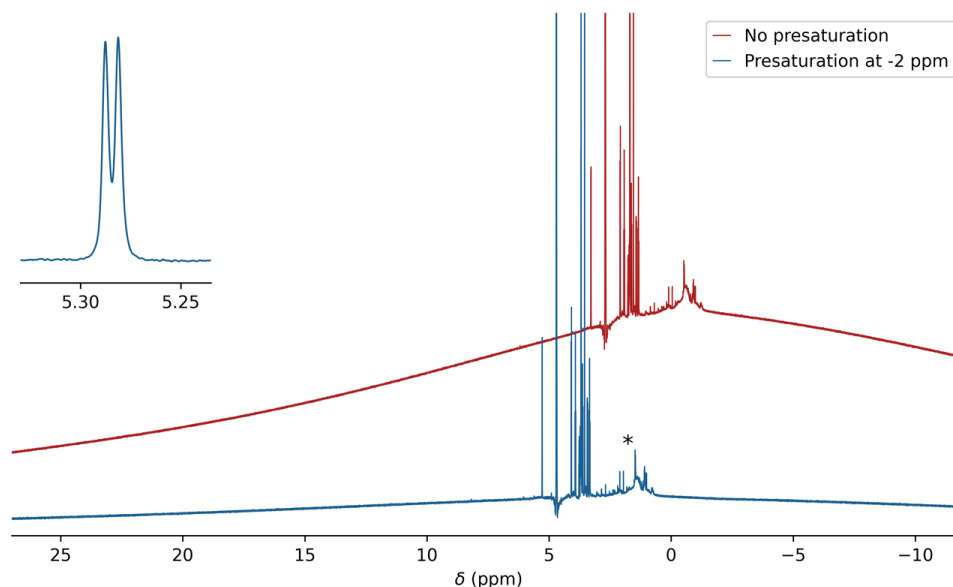
275 A sagittal ( $xz$ ) cross-section through the absorption mode 3D image of the cell, recorded  
276 on a Bruker Neo 800-MHz instrument equipped with a 3-axis pulsed field gradient  
277 probehead, yielded a shape that matched the ellipsoidal design (Figure 4C) but that did not  
278 include the access channel because the solvent in that channel falls outside the RF coil.  
279 Small distortions near the bottom of the image correspond to the drop off in RF coil



- 13 -

280 receptivity. Distortions at the top of the sample originate from the access channel which  
281 also distorts the ellipse. However, cross-sections taken through the 3D image along the x  
282 and z axis through the center of the sample, plotted along the sides of the 3D image, show  
283 the expected nearly rectangular shape, indicative of linear imaging gradients.

284  $^1\text{H}$  non-spinning linewidths of  $\sim 1$  Hz at half height (600 MHz) obtained with the cell  
285 (expanded anomeric doublet in Fig.5) were slightly larger than those obtained for a regular  
286 5-mm NMR sample in the same probehead. With a width of only  $\sim 13$  Hz at 0.55% of the  
287 HDO peak height the lineshape is also very good, which is most important for protein NMR  
288 studies, where protein  $^1\text{H}$  line widths at half height commonly exceed 10-20 Hz due to fast  
289 transverse relaxation and the absence of a “hump” in the water line shape is critical for  
290 good solvent suppression.



291  
292 **Figure 5.**  $^1\text{H}$  background of printed microcell. The regular  $^1\text{H}$  NMR spectrum of a 1 mg/mL solution  
293 of sucrose in 99%  $\text{D}_2\text{O}$ , recorded without presaturation (red) and with  $^1\text{H}$  presaturation at -2 ppm  
294 (blue), using a 100 Hz RF field strength to suppress the  $^1\text{H}$  background of the solid resin.  
295 Resonances from small impurities released from the printed cell are marked with an asterisk. For  
296 display purposes, the not-presaturated spectrum has been shifted upfield by 2 ppm and offset  
297 vertically. The inset shows the splitting for the sucrose anomeric doublet at 5.29 ppm.

298



- 14 -

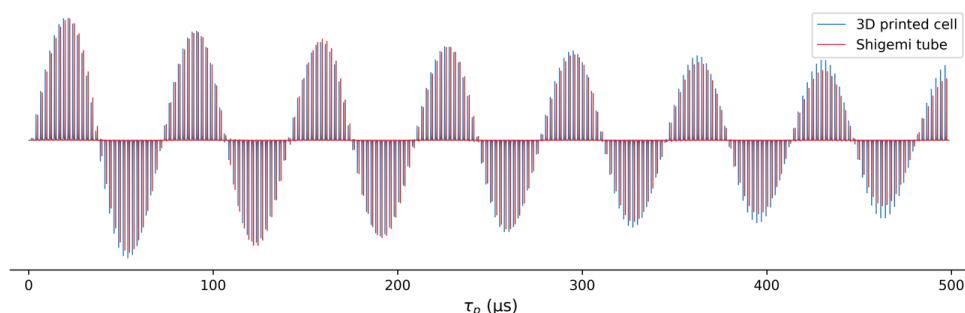
299 We note that sometimes microscopic air bubbles can form inside the cell after filling it with  
300 the NMR sample solution. When this happens, it has a very strong adverse impact on both  
301 lineshape and linewidth. To eliminate the potential presence of such air bubbles, we briefly  
302 (~20 sec) spin the filled sample cell in a speedvac, operating at a pressure of *ca* 150 Pa,  
303 and replenish any lost volume by adding a few  $\mu\text{L}$  of the protein solution to the access  
304 channel.

305 For observation of simple one-dimensional  $^1\text{H}$  spectra, without echo delays, the protons of  
306 the resin yield a strong background signal that is broad due to the rapid transverse  
307 relaxation of this solid material. This background signal is readily suppressed by spin echo  
308 delays prior to the start of signal acquisition, as are already present in nearly all protein  
309 NMR experiments. It can also be effectively reduced by presaturating this broad  
310 background with a weak RF field outside the spectral region of interest. Saturation with a  
311 100-Hz RF field, applied at -2 ppm in the  $^1\text{H}$  spectrum, attenuates the background signal  
312 by about six-fold (Figure 5).

313 The  $^1\text{H}$  RF field homogeneity was compared for the microcell and for a Shigemi sample  
314 (straight wall) containing 280  $\mu\text{L}$  of phosphate buffered saline (PBS) solution in 99%  $\text{D}_2\text{O}$ .  
315 Due to the substantial detuning of the 600 MHz cryoprobe used for this work by the ionic  
316 solution in the Shigemi sample, the RF power for this sample was increased by 2.7 dB over  
317 the power used for the microcell to yield the same  $90^\circ$  pulse width of  $\sim 17 \mu\text{s}$ . Comparison  
318 of the decay of the signal when the excitation pulse is increased from 0.2 to 497.7  $\mu\text{s}$  using  
319 the Bruker “paropt” module (Figure 6) shows slightly better RF field homogeneity for the  
320 smaller 3D printed microcell than for the Shigemi sample. Notably, the intensity of the  
321 signal after a  $90^\circ$  pulse was only  $\sim 10\%$  lower for the printed microcell than for the Shigemi  
322 tube that contained more than double the volume of the same solution.



- 15 -



323  
324 **Figure 6.** Comparison of  $^1\text{H}$  RF field homogeneity in a 280- $\mu\text{L}$  Shigemi sample cell (red) and in the  
325 3D printed 130- $\mu\text{L}$  23 $\times$ 3.3-mm ellipsoidal microcell (blue). Signal intensity is shown as a function  
326 of  $^1\text{H}$  pulse duration, ranging from 0.2 to 497.7  $\mu\text{s}$ , generated by the Bruker macro 'paropt'. Both  
327 samples contained the same solution of PBS buffer in 99%  $\text{D}_2\text{O}$ . The RF power for the microcell  
328 sample was adjusted 2.7 dB lower than for the Shigemi sample to equalize the 90° pulse lengths.

329

### 330 2.6 Observation of high-resolution protein NMR spectra

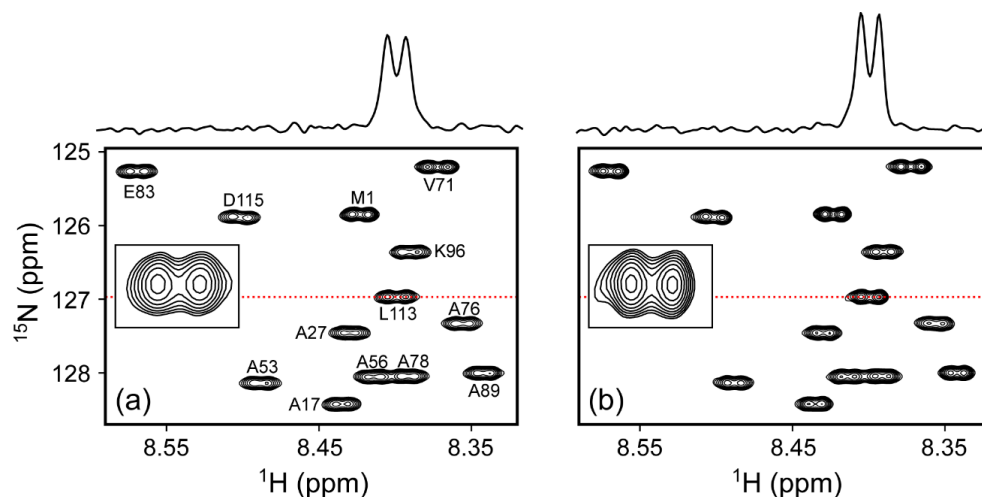
331 The high resolution and sensitivity obtained with the microcell are illustrated for two  
332 proteins, N-acetylated  $\alpha$ -synuclein and native C-terminal amidated melittin in its  
333 monomeric and tetrameric forms. Complete or nearly complete N-acetylation of  $\alpha$ -  
334 synuclein is invariably present in mammalian cells (Bartels et al., 2011) and strongly  
335 impacts its interaction with phospholipids (Kang et al., 2012; Maltsev et al., 2012). By  
336 simultaneously including a plasmid for expressing the NatB complex, needed for  
337 acetylation of  $\alpha$ -synuclein, together with a plasmid for  $\alpha$ -synuclein, fully N-acetylated  
338 protein can also be obtained from bacterial expression systems (Johnson et al., 2010).  
339 Although this combined expression reduced protein yields in our hands, it enabled the  
340 pivotal incorporation of stable isotopes, such as  $^{15}\text{N}$ , in the biologically relevant state of  
341 the protein.

342 As can be seen, in *ca* 20 min, a high-quality gradient-enhanced  $^1\text{H}$ - $^{15}\text{N}$  HSQC spectrum  
343 was obtained for 130  $\mu\text{g}$  of N-acetylated  $\alpha$ -synuclein (14.5 kDa) in PBS buffer, pH 6.5,  
344 when using the microcell, which approaches the sensitivity and resolution that was



- 16 -

345 obtained for 500  $\mu\text{g}$  protein in a regular 5-mm sample cell, using a 0.5 mL sample volume  
346 (Figure 7).



347

348 **Figure 7.** Comparison of small regions of the 600-MHz  $^1\text{H}$ - $^{15}\text{N}$  HSQC spectra of 70  $\mu\text{M}$  N-acetylated  
349  $\alpha$ -synuclein at 20  $^\circ\text{C}$  in PBS-buffer, pH 6.5. Each spectrum results from  $175^* \times 4000^*$  data points  
350 with two transients per FID, for total measuring times of 21 min each. (A) 130  $\mu\text{L}$  in the 3D printed  
351 microcell; (B) 500  $\mu\text{L}$  in a standard 5-mm NMR tube. Lowest contours are drawn at the same level  
352 above the respective RMS noise. Insets show the expansion of the L113 cross peak, with cross-  
353 sections through L113 above the panels at locations marked by the red dotted lines. The  
354 comparison shows slightly lower resolution of the  $^1\text{H}^{\text{N}}\text{-}^1\text{H}^{\alpha}$  doublets for the microcell, reflected in  
355 12% lower S/N versus 6.5% lower peak integrals relative to RMS noise.

356 The utility of the microcell becomes even more compelling for the study of the  
357 tetramerization of native melittin, which requires C-terminal amidation. The latter involves  
358 a large number of chemical derivatization and purification steps (Gelenter and Bax, 2023),  
359 making it very challenging to generate adequate quantities of peptide for driving it to its  
360 tetrameric state within a standard 5-mm NMR tube. Tetramerization is promoted by  
361 increasing the NaCl concentration, but the tuning of the RF circuitry in cryoprobes often  
362 limits salt concentrations to be below *ca* 0.5 M. Here, we demonstrate that the microcell  
363 enables observation of the monomer-tetramer equilibrium at salt concentrations of 2 M,  
364 and that indeed even at a moderate peptide concentration of 250  $\mu\text{M}$  the peptide is fully  
365 tetrameric in the presence of 2 M NaCl (Figure 8). Interestingly, residues L9-R24, close  
366 to the center of the peptide, are attenuated by an exchange process that is much less

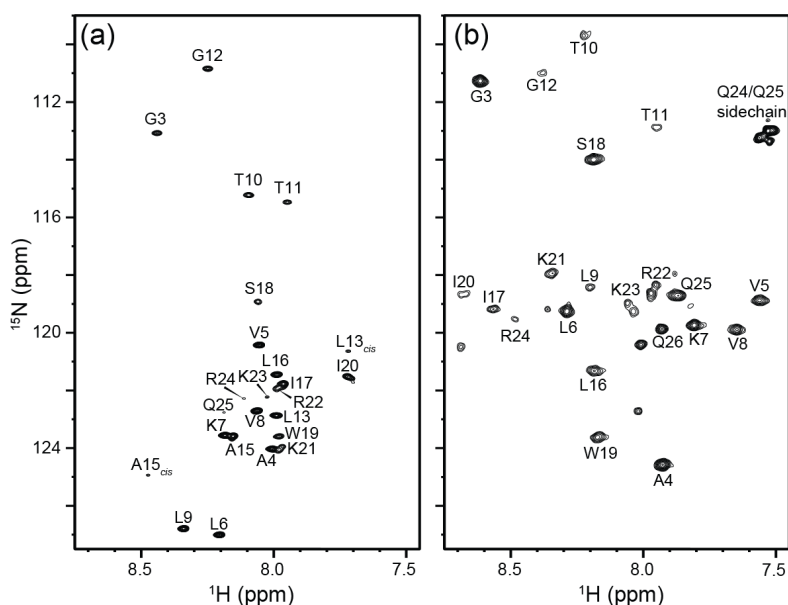




- 17 -

367 prevalent at low ionic strength and high peptide concentration (Gelenter et al., 2024). We  
368 speculate that the line-broadening associated with these weaker resonances arises from the  
369 exchange process between the asymmetric arrangement of the two dimers seen in its X-ray  
370 tetrameric structure (Terwilliger and Eisenberg, 1982) switching from fast exchange at  
371 lower ionic strength to intermediate exchange at 2 M NaCl.

372 Notably, the same microcell was used for the two melittin spectra. After recording of the  
373 low-ionic strength spectrum, contents of the microcell was removed and used to dissolve  
374 15.2 mg NaCl, prior to insertion of the high ionic strength sample into the original cell,  
375 thereby demonstrating the recyclability of the tube.



376

377 **Figure 8.** 800-MHz  $^1\text{H}$ - $^{15}\text{N}$  HSQC spectra from 90  $\mu\text{g}$  (250  $\mu\text{M}$ ) of  $^{15}\text{N}$ -labeled native melittin in a  
378 130- $\mu\text{L}$  microcell. Both spectra were collected at 288 K in 10 mM sodium phosphate buffer, pH  
379 7.0, containing 3%  $\text{D}_2\text{O}$ . (A) Sample containing no NaCl, where melittin remains an intrinsically  
380 disordered monomer. L13<sub>cis</sub> and A15<sub>cis</sub> correspond to residues in monomers with P14 in the  
381 *cis* conformation. The data was collected with 2 transients per FID, using 200\* points in the  
382 indirect dimension corresponding to an evolution of 103 ms and a total measurement time of 27  
383 min. (B) 15.2 mg of NaCl was added to the sample from (A) to reach a final concentration of 2 M  
384 NaCl. Under these conditions melittin adopts an  $\alpha$ -helical tetrameric conformation. The data was  
385 collected with 8 transients, using 100\* points in the indirect dimension ( $t_{1,\text{max}} = 51$  ms) and a total  
386 experimental time of 52 min.



- 18 -

387 **3 Concluding remarks**

388 3D printing enables the efficient and relatively inexpensive creation of complex,  
389 customized products with minimal waste. It is extensively used for prototyping new  
390 designs of items with intricate or complex geometries and has broad impact in science and  
391 engineering. 3D printing also enabled the design and construction of high performance  
392 solid-state NMR probes, offering similar or improved filling factors due to the coil being  
393 in close proximity to the sample, resulting in high RF transmit and receive efficiencies  
394 (Long et al., 2021;Pereira et al., 2023).

395 In solution NMR spectroscopy, 3D-printed bioreactor platforms were introduced that are  
396 compatible with low-field NMR spectrometers that accommodate bioengineered 3D cell  
397 models (Mangas-Florencio et al., 2025). That work consisted of a bioreactor made of  
398 biocompatible materials and included a microfluidic system for optimization of cell culture  
399 conditions during the actual NMR data collection process.

400 The application of 3D printing to high-field solution NMR spectroscopy has remained  
401 rather limited, largely due to the requirements of high magnetic field homogeneity and  
402 minimal background signals. Our study demonstrates that the homogeneity requirement  
403 can be met by printing small sample cells with an ellipsoidal shape. The half-height line  
404 widths achievable for our microcell is *ca* 1 Hz and remains limited by the precision at  
405 which the cell's surface can be printed. For shimming purposes, we first used Bruker's  
406 topshim program to adjust field homogeneity to starting values on a regular solution NMR  
407 sample filled to the same height (~40 mm) as the length of the microcell. Subsequently,  
408 after entering the microcell into the magnet, we used topshim followed by iterative tuning  
409 of  $z$ ,  $z^2$ ,  $x$ ,  $y$ ,  $xz$  and  $yz$  gradients. The microcells can easily be recycled as they slide in  
410 and out of standard high-quality Wilmad-507, New Era NE-HP5, or Norell Standard Series  
411 5-mm NMR tubes. The access channel of the microcell is sufficiently small that surface  
412 tension prevents the aqueous solution from leaving the microcell when the 5-mm NMR  
413 tube is fully inverted while the microcell slides out of it.

414 Although inexpensive, sample cells are easily recycled as highlighted for the melittin  
415 sample, where 15.2 mg of salt was added to the initial sample by first removing the sample



- 19 -

416 solution, dissolving the NaCl, and re-injecting the solution into the original cell, all with  
417 minimal losses. It is advisable to briefly spin and expose the sample to vacuum to remove  
418 dissolved gasses, in particular for lengthy experiments. Formation of even microscopic air  
419 bubbles deteriorates homogeneity for the microcell sample more than for the Shigemii or  
420 larger conventional NMR sample tubes.

421 The sample cell appears unsuitable for the use of organic solvents which dissolve and  
422 release resin components, resulting in strong narrow background signals. Even when using  
423 water as the solvent, slowly increasing signals from micromolar quantities of resin-derived  
424 small molecules appear in the  $^1\text{H}$  spectrum over a period of days (marked by an asterisk in  
425 Figure 5). However, the standard use of isotope-enriched multi-dimensional multinuclear  
426 NMR experiments keeps these resonances well below the signal-to-noise threshold level,  
427 and unless such contaminants have a strong interaction with the protein studied they have  
428 no effect on the acquired spectra.

429 We cleaned the microcells by soaking them overnight at 60 °C in milli-Q water and  
430 subsequent removal of most of the solvent with a standard gel micropipette tip that didn't  
431 quite reach the bottom of the cell, followed by upside down centrifugation after insertion  
432 into an Eppendorf tube to remove the remainder of the solvent. An additional rinse with  
433 130  $\mu\text{L}$   $\text{D}_2\text{O}$ , followed by centrifugation and vacuum exposure can be used to remove any  
434 residual solvent protons if the sample is intended for measurements in highly deuterated  
435  $\text{D}_2\text{O}$ . These are the most labor-intensive steps in preparing the sample cells, but limited  
436 quantities of unrinsed sample cells are available upon request.

437

#### 438 **4. Methods**

##### 439 4.1 Magnetic susceptibility measurements

440 Selective excitation while applying a 11.5 G/cm (20% on the Bruker Neo-600 instrument)  
441 was used for collecting the HDO solvent resonance measurements (Appendix A1) of 0.6-  
442 mm thickness slices at various heights,  $h$ , above the flat interface between a solid printed  
443 plug and the aqueous solvent. The printed plug with outer diameter of 4-mm and a length



- 20 -

444 of 20-mm, including its hemispheric bottom, was inserted and pushed to the bottom of a  
445 regular NMR tube, prefilled with 0.7 mL of 97% D<sub>2</sub>O or 97% H<sub>2</sub>O solution. A similar tube  
446 without the plug was filled to the same height with the same solution and used for shimming  
447 the magnetic field using topshim prior to inserting the sample with the plug at its bottom,  
448 where the same shim settings of the sample without the plug were used.. The thickness of  
449 the aqueous fraction of the slice collected for  $h=0$  was two-fold smaller than for slices at  
450  $h>0.3$  mm, with a correspondingly lower integrated volume. The frequency of slices  
451 collected at heights  $>\sim 10$  mm above the plug became essentially independent of  $h$ . The  
452 slice collected at  $h=0$  shows extensive line broadening due to the large field gradient at the  
453 solvent-plug interface (Figure 2A-C). The difference in ppm frequency was used as a  
454 measure for  $(\chi_{\text{solvent}} - \chi_{\text{resin}})/2$ .

#### 455 4.2 Printing of the microcell

456 Cells were printed in Clear V4 resin on a Form 3+ printer at 25-micron resolution to achieve  
457 a smooth surface finish. The designs were created in OpenSCAD (2021.01) using standard  
458 STL export settings, then prepared for printing in PreForm (3.43.2). Models were oriented  
459 so that the bottom of each cell faced downward on the build platform, with 0.2 mm  
460 touchpoint supports attached only at the bottom of the cells. The cells were washed with  
461 isopropyl alcohol (IPA) and UV-cured using Form Cure for 16 hours at 60 °C.  
462 Subsequently, cells were filled with Milli-Q water and immersed in a water-filled falcon  
463 tube that was heated at 60 °C for 12 hours to remove water-soluble components. After  
464 removal of the water from the cells by pipetting followed by centrifugation upside down  
465 in Eppendorf tubes, they were briefly dried under vacuum.

466 For doping studies, plugs were first printed on an ELEGOO Saturn 4 Ultra printer using  
467 transparent ABS-like Resin V3. The designs were created in OpenSCAD (2021.01) with  
468 standard STL export settings and prepared for printing in CHITUBOX (2.2). Printing was  
469 performed with a 50-micron layer height and an exposure time of 3.5 seconds per layer.  
470 After printing, the plugs were thoroughly washed with IPA and cured for 5 minutes at room  
471 temperature using a Mercury SX curing station. The doped resin was prepared by mixing  
472 ABS-like Resin V3 with a cobalt(II) bis(2-ethylhexanoate) solution (199.47 g, 65 wt.% in  
473 mineral spirits, Sigma-Aldrich, 444545) on a shaker at 37 °C and 200 rpm for 30 minutes.



- 21 -

474 Cells printed on the FormLabs printer using Clear V4 resin with 2- and 5-mM cobalt(II)  
475 doping revealed comparable performance to the undoped cells, and doping therefore was  
476 not pursued further.

477

#### 478 4.3 NMR sample preparation

479 The microcells were filled to the top with the sample solution (~130  $\mu$ L) using a gel-tip  
480 pipette and degassed at *ca* 150 Pa pressure for 20-30 seconds using a SpeedVac (Savant,  
481 SVC-100-H). After degassing, the cells were topped off with *ca* 2  $\mu$ L of additional sample  
482 solution and inserted into standard Wilmad-507, New Era NE-HP5, or Norell Standard  
483 Series 5-mm NMR tubes.

#### 484 4.4 Imaging of the microcell

485 Although MRI normally uses absolute value mode displays, higher resolution absorption  
486 mode spectra can also be obtained (Bretthorst, 2008). For generating images of the  
487 microcell, we used a very simple one-pulse sequence with variable durations of the x, y,  
488 and z gradients for encoding the three spatial dimensions (Appendix A3). The experiment  
489 used Rance-Kay quadrature selection (Palmer et al., 1991; Kay et al., 1992) in both the x  
490 and y dimensions, by collecting four scans per hypercomplex time domain data point  
491 ( $n_s=1$ ). NMRPipe (Delaglio et al., 1995) processing of the 3D time domain matrix was  
492 used to generate regular, amplitude-modulated quadrature (States et al., 1982) in both  
493 indirect dimensions (see Appendix A4 for NMRPipe processing script). A total of  $20*(x) \times$   
494  $20*(y) \times 512*(z)$  data points were collected with a total acquisition time of *ca* 9 minutes  
495 for a sample that contained 1.8 mM  $\text{CuCl}_2$  in 99%  $\text{D}_2\text{O}$ .

496

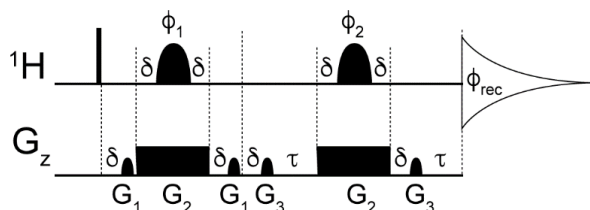


- 22 -

## 497 Appendix A: Supplementary data and code

498

### 499 A1: Pulse diagram used for slice selection

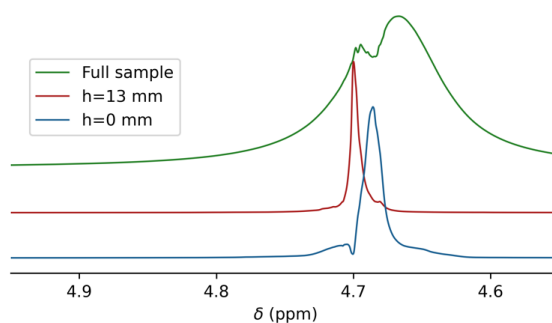


500

501 **Figure A1.** Diagram of the slice selection pulse sequence used to measure magnetic  
502 susceptibility. The narrow bar represents the 90  $^1\text{H}$  excitation pulse. The shaped pulses  $\phi_1$  and  
503  $\phi_2$  have a profile of Reburp (Geen and Freeman, 1991) with a duration of 2 ms and a variable  
504 offset frequency, ranging from ca +23 to -30 kHz from the water signal resonating at 4.7 ppm.  
505 The gradient pulses are either sine-bell shaped or rectangular, with durations of 0.5, 2.1 and  
506 0.5 ms and a strength of 2, -11.5 and 3.5 Gauss/cm for  $G_1$ ,  $G_2$  and  $G_3$ , respectively. Delays:  $\delta$   
507 = 50  $\mu\text{s}$  and  $\tau$  = 60  $\mu\text{s}$ . The following phase cycling scheme was used:  $\phi_1$  = y, y, y, y, -x, -x, -x, -x,  
508 -y, -y, -y, -y, x, x, x, x;  $\phi_2$  = x, y, -x, -y;  $\phi_{\text{rec}}$  = x, -x, x, -x, -x, x, -x, x. The interscan delay was set to 4  
509 s, number of scans to 4, spectral width to 8620 Hz and the acquisition time to 2 s.

510

### 511 A2: Spectra used for measuring $\chi_{\text{glass}} - \chi_{\text{H}_2\text{O}}$



512

513 **Figure A2.** Same as Figure 1B (main text), but for a solution containing 97%  $\text{H}_2\text{O}$ /3%  $\text{D}_2\text{O}$ . The  
514 resonance of the full Shigemi tube sample (green) is broadened by radiation damping and  
515 shown together with slices taken at  $h = 0$  mm (blue), and at  $h = 13$  mm (red). The center of the  
516 green resonance is shifted relative to its regular position due to radiation damping effect in  
517 the deliberately mistuned probe (Torchia, 2009).



- 23 -

518 **A3: Bruker pulse program used for imaging the microcell:**

```
519 #include<Avance.incl>
520 #include<Grad.incl>
521 #include<De.incl>
522
523
524 "d11=30m"
525
526 "in0=inf1". ;125u
527 "in10=inf2" ;125u
528
529 "d0=0"
530 "d10=0"
531
532 define list<gradient> EA2 = { 1.000 -1.000}
533
534 aqseq 321
535
536
537 1 ze
538 1m
539 2 d11 groff
540 10u BLKGRAD
541 10u p19:f1 ;set to 1000dB unless presat is needed
542 10u fq=cnst2(bf ppm):f1 ;chemical shift for the resin to be
543 presat'ed
544 d1 cw:f1
545 10u do:f1
546 10u UNBLKGRAD
547 p20:gp20. ;3m at 33% of z-grad
548 1m fq=0:f1 ;shift carrier back to be on-resonance with water
549 1m p11:f1
550 (p1 ph1):f1 ;20 degree flip angle
551 1u gron1*EA ;x-grad 8%
552 d0
553 1u groff
554
555 1u gron2*EA2 ;y-grad 8%
556 d10
557 1u groff
558 600u ;delay to dephase a very broad hump
559 1u gron3 ;z-grad -1%
560 go=2 ph31
561 d11 groff mc #0 to 2
562 F1EA(calgrad(EA), caldel(d0)) ;TD1=40
563 F2EA(calgrad(EA2), caldel(d10)) ;TD2=40
564 d11 BLKGRAD
565 exit
566
567
568 ph1=0
569 ph31=0
```



- 24 -

#### 570 A4: NMRPipe conversion and processing scripts

```
571 #!/bin/csh
572
573 bruk2pipe -verb -in ./ser \
574   -bad 0.0 -ext -aswap -DMX -decim 1240 -dspfvS 20 -grpdy 68 -ws 8 -
575 noi2f \
576   -xN          1024 -yN          40 -zN          40
577 \
578   -xT          512 -yT          20 -zT          20
579 \
580   -xMODE       DQD -yMODE       Echo-AntiEcho -zMODE       Echo-AntiEcho
581 \
582   -xSW         16129.032 -ySW         8000.000 -zSW         8000.000
583 \
584   -xOBS        800.134 -yOBS        800.134 -zOBS        800.134
585 \
586   -xCAR        4.821 -yCAR        4.821 -zCAR        4.821
587 \
588   -xLAB        Hz -yLAB        Hy -zLAB        Hx
589 \
590   -ndim        3 -aq2D          Complex
591 \
592 | pipe2xyz -x -out ./fid/test%03d.fid -ov
593
594
595 xyz2pipe -in fid/test%03d.fid -x \
596 | nmrPipe -fn SP -off 0.5 -end 0.98 -pow 2 -c 0.5 \
597 | nmrPipe -fn ZF -zf 2 -auto \
598 | nmrPipe -fn FT \
599 | nmrPipe -fn PS -p0 149 -p1 38 -di \
600 | nmrPipe -fn TP \
601 | nmrPipe -fn SP -off 0.5 -end 0.98 -pow 1 -c 0.5 \
602 | nmrPipe -fn ZF -zf 2 -auto \
603 | nmrPipe -fn FT \
604 | nmrPipe -fn PS -p0 135 -p1 0 -di \
605 | nmrPipe -fn ZTP \
606 | nmrPipe -fn SP -off 0.5 -end 0.98 -pow 1 -c 0.5 \
607 | nmrPipe -fn ZF -zf 2 -auto \
608 | nmrPipe -fn FT \
609 | nmrPipe -fn PS -p0 90 -p1 0 -di \
610 | nmrPipe -fn TP \
611 | nmrPipe -fn POLY -ord 4 -nw 300 -nl 301 1740 \
612 | pipe2xyz -out ft/test%04d.ft3 -x -ov -verb
613
```





- 25 -

## 614 Author contributions

615 TK: conceptualization (equal), 3D printing and cleaning, figures 1-6, review and editing  
616 (equal). MDG: review and editing (equal), data collection (equal), figure 8. JY: review and  
617 editing (equal), data collection (equal), figure 7. AB: conceptualization (equal), writing  
618 original draft, review and editing (equal), recording data (equal).

## 619 Acknowledgments

620 This work was supported by the Intramural Research Program of the NIDDK at the  
621 National Institutes of Health. We thank James L. Baber for assistance with  
622 instrumentation, and Philip Anfinrud, Marshall J. Smith, Nico Tjandra and David A.  
623 Nyenhuis for useful suggestions.

## 624 Competing interests

625 AB is a member of the editorial board of *Magnetic Resonance*.  
626 The authors have no other competing interests to declare.  
627

## 628 Financial support

629 This research was supported by grant DK029046 from the Intramural Research Program  
630 of the National Institute of Diabetes and Digestive and Kidney Diseases.

631

632

## 633 References

634

635  
636 Bartels, T., Choi, J. G., and Selkoe, D. J.: alpha-Synuclein occurs physiologically as a  
637 helically folded tetramer that resists aggregation, *Nature*, 477, 107-U123,  
638 10.1038/nature10324, 2011.

639 Bretthorst, G. L.: Automatic phasing of MR images. Part II: Voxel-wise phase estimation,  
640 *J. Magn. Reson.*, 191, 193-201, 10.1016/j.jmr.2007.12.011, 2008.



- 26 -

- 641 Delaglio, F., Grzesiek, S., Vuister, G. W., Zhu, G., Pfeifer, J., and Bax, A.: NMRPipe: a  
642 multidimensional spectral processing system based on UNIX pipes., *J. Biomol. NMR*, 6,  
643 277-293, 1995.
- 644 Evans, D. F.: The determination of the paramagnetic susceptibility of substances in  
645 solution by nuclear magnetic resonance, *J. Chem. Soc.*, 2003-2005,  
646 10.1039/jr9590002003, 1959.
- 647 Freeman, R., Kempell, S. P., and Levitt, M. H.: Radiofrequency pulse sequences which  
648 compensate their own imperfections, *J. Magn. Reson.*, 38, 453-479, 1980.
- 649 Geen, H., and Freeman, R.: Band-selective radiofrequency pulses, *J. Magn. Reson.*, 93, 93-  
650 141, 1991.
- 651 Gelenter, M., and Bax, A.: Recombinant Expression and Chemical Amidation of  
652 Isotopically Labeled Native Melittin, *J. Am. Chem. Soc.*, 145, 3850-3854, 2023.
- 653 Gelenter, M. D., Yau, W. M., Anfinrud, P. A., and Bax, A.: From Milliseconds to Minutes:  
654 Melittin Self-Assembly from Concerted Non-Equilibrium Pressure-Jump and Equilibrium  
655 Relaxation Nuclear Magnetic Resonance, *J. Phys. Chem. Lett.*, 15, 1930-1935,  
656 10.1021/acs.jpcclett.3c03563, 2024.
- 657 Gutiérrez-Mejía, F., and Ruiz-Suárez, J. C.: AC magnetic susceptibility at medium  
658 frequencies suggests a paramagnetic behavior of pure water, *Journal of Magnetism and*  
659 *Magnetic Materials*, 324, 1129-1132, 10.1016/j.jmmm.2011.10.035, 2012.
- 660 Hizawa, T., Takahashi, M., and Iwase, E.: Sample shape design for a micro-volume NMR  
661 spectroscopy, *Micro & Nano Letters*, 12, 550-553, 10.1049/mnl.2017.0138, 2017.
- 662 Hoffman, R.: Magnetic susceptibility measurement by NMR: 2. The magnetic  
663 susceptibility of NMR solvents and their chemical shifts, *J. Magn. Reson.*, 335,  
664 10.1016/j.jmr.2021.107105, 2022.
- 665 Hoffman, R. E.: Magnetic susceptibility measurement by NMR: 1. The temperature  
666 dependence of TMS, *J. Magn. Reson.*, 312, 10.1016/j.jmr.2020.106689, 2020.
- 667 Johnson, M., Coulton, A. T., Geeves, M. A., and Mulvihill, D. P.: Targeted Amino-  
668 Terminal Acetylation of Recombinant Proteins in *E. coli*, *PLoS One*, 5, e15801, e15801  
669 10.1371/journal.pone.0015801, 2010.
- 670 Kang, L., Moriarty, G. M., Woods, L. A., Ashcroft, A. E., Radford, S. E., and Baum, J.: N-  
671 terminal acetylation of alpha-synuclein induces increased transient helical propensity and  
672 decreased aggregation rates in the intrinsically disordered monomer, *Protein Sci.*, 21, 911-  
673 917, 10.1002/pro.2088, 2012.
- 674 Kay, L. E., Keifer, P., and Saarinen, T.: Pure absorption gradient-enhanced heteronuclear  
675 single quantum correlation spectroscopy with improved sensitivity, *J. Am. Chem. Soc.*,  
676 114, 10663-10665, 1992.
- 677 Long, Z., Ruthford, J., and Opella, S. J.: 3D printed sample tubes for solid-state NMR  
678 experiments, *J. Magn. Reson.*, 327, 10.1016/j.jmr.2021.106957, 2021.
- 679 Maltsev, A. S., Ying, J. F., and Bax, A.: Impact of N-Terminal Acetylation of  $\alpha$ -Synuclein  
680 on Its Random Coil and Lipid Binding Properties, *Biochemistry*, 51, 5004-5013, 2012.
- 681 Mangas-Florencio, L., Herrero-Gómez, A., Eills, J., Azagra, M., Batlló-Rius, M., and  
682 Marco-Rius, I.: A DIY Bioreactor for in Situ Metabolic Tracking in 3D Cell Models via  
683 Hyperpolarized  $^{13}\text{C}$  NMR Spectroscopy, *Anal. Chem.*, 97, 1594-1602,  
684 10.1021/acs.analchem.4c04183, 2025.



- 27 -

- 685 Manu, V. S., Olivieri, C., and Veglia, G.: AI-designed NMR spectroscopy RF pulses for  
686 fast acquisition at high and ultra-high magnetic fields, *Nature Communications*, 14,  
687 10.1038/s41467-023-39581-4, 2023.
- 688 Palmer, A. G., Cavanagh, J., Wright, P. E., and Rance, M.: Sensitivity Improvement in  
689 Proton-Detected 2-Dimensional Heteronuclear Correlation Nmr-Spectroscopy, *J. Magn.*  
690 *Reson.*, 93, 151-170, 1991.
- 691 Pereira, D., Sardo, M., Marín-Montesinos, I., and Mafra, L.: One-Shot Resin 3D-Printed  
692 Stators for Low-Cost Fabrication of Magic-Angle Spinning NMR Probeheads, *Anal.*  
693 *Chem.*, 95, 10384-10389, 10.1021/acs.analchem.3c01323, 2023.
- 694 Roschmann, P.: Radiofrequency penetration and absorption in the human body -  
695 Limitations to high-field whole-body nuclear magnetic resonance imaging, *Med. Phys.*, 14,  
696 922-931, 1987.
- 697 Sangal, M., Anikeeva, M., Priese, S. C., Mattern, H., Hövener, J. B., and Speck, O.: MR  
698 based magnetic susceptibility measurements of 3D printing materials at 3 Tesla, *Journal of*  
699 *Magnetic Resonance Open*, 16-17, 10.1016/j.jmro.2023.100138, 2023.
- 700 Schenck, J. F.: The role of magnetic susceptibility in magnetic resonance imaging: MRI  
701 magnetic compatibility of the first and second kinds, *Med. Phys.*, 23, 815-850,  
702 10.1118/1.597854, 1996.
- 703 States, D. J., Haberkorn, R. A., and Ruben, D. J.: A Two-dimensional Nuclear Overhauser  
704 Experiment with Pure Absorption Phase in Four Quadrants, *J. Magn. Reson.*, 48, 286-292,  
705 1982.
- 706 Stott, K., Stonehouse, J., Keeler, J., Hwang, T. L., and Shaka, A. J.: Excitation sculpting in  
707 high-resolution nuclear magnetic resonance spectroscopy - Application to selective NOE  
708 experiments, *J. Am. Chem. Soc.*, 117, 4199-4200, 10.1021/ja00119a048, 1995.
- 709 Terwilliger, T. C., and Eisenberg, D.: The structure of melittin. 2. Interpretation of the  
710 structure, *J. Biol. Chem.*, 257, 6016-6022, 1982.
- 711 Torchia, D. A.: Slight mistuning of a cryogenic probe significantly perturbs the water H-1  
712 precession frequency, *J. Biomol. NMR*, 45, 241-244, 10.1007/s10858-009-9363-6, 2009.
- 713 Tsukada, K., Kiwa, T., and Masuda, Y.: AC magnetic properties of large volume of water  
714 - Susceptibility measurement in unshielded environment, *Japanese Journal of Applied*  
715 *Physics Part 2-Letters & Express Letters*, 45, L1097-L1099, 10.1143/jjap.45.L1097, 2006.
- 716 Ugurbil, K.: Imaging at ultrahigh magnetic fields: History, challenges, and solutions,  
717 *Neuroimage*, 168, 7-32, 10.1016/j.neuroimage.2017.07.007, 2018.
- 718 VanderHart, D. L.: Magnetic Susceptibility & High Resolution NMR of Liquids and  
719 Solids, in: *Encyclopedia of Nuclear Magnetic Resonance*, edited by: Grant, D. M., and  
720 Harris, R. K., Wiley, New York, 2938-2945, 1996.
- 721 Xia, Y. L., Rossi, P., Subrahmanian, M. V., Huang, C. D., Saleh, T., Olivieri, C.,  
722 Kalodimos, C. G., and Veglia, G.: Enhancing the sensitivity of multidimensional NMR  
723 experiments by using triply-compensated  $\pi$  pulses, *J. Biomol. NMR*, 69, 237-243,  
724 10.1007/s10858-017-0153-2, 2017.
- 725